

Structure of gaps induced by retrograde satellites embedded in accretion discs

F. J. Sánchez-Salcedo^{1*} and A. Santillán²

¹Universidad Nacional Autónoma de México, Instituto de Astronomía, A.P. 70-264, 04510, Ciudad de México, Mexico

²Departamento de Supercómputo, Dirección General de Cómputo y de Tecnologías de Información y Comunicación, Universidad Nacional Autónoma de México, Ciudad Universitaria, 04510, Ciudad de México, Mexico

Accepted XXX. Received YYY; in original form ZZZ

ABSTRACT

Using 2D simulations, we investigate how a non-accreting satellite on a fixed retrograde circular orbit affects the structure of the accretion disc in which it is embedded. We vary the satellite-to-primary mass ratio q , the disc viscosity ν , and the inner boundary conditions. A viscous criterion for gap opening is derived, which is broadly consistent with the simulations. We find a scaling relation of the gap depth with q and ν . Unlike the prograde case, the satellite is located at the gap’s inner edge, resulting in a surface density at the satellite’s orbital radius up to 20 times higher than at the gap’s minimum. As the viscosity decreases, the gap depth increases, while the radial shift of the gap and the satellite’s orbital radius decreases. Gap-opening satellites may drive radial motions in the disc, producing eccentric gaps. Positioned at the gap edge, satellites experience a rapidly fluctuating environment. Migrating satellites can develop orbital eccentricities comparable to the disc’s aspect ratio. In a 3D simulation with $q = 0.01$, the flow velocity exhibits a notorious vertical component in the gap’s inner edge. A comparison between 2D and 3D simulations reveals a slight radial offset in gap position, resulting in a lower surface density at the perturber’s orbital radius in the 3D simulation.

Key words: accretion, accretion discs – black hole physics – galaxies: active – galaxies: kinematics and dynamics – hydrodynamics

1 INTRODUCTION

The accretion discs of active galactic nuclei (AGNs) can host stellar-mass black holes (BHs) (e.g., Tagawa et al. 2023, and references therein). In fact, the AGN accretion disc are commonly immersed in a nuclear star cluster and a fraction of the initial stellar-mass BH population of this cluster can be captured by the disc (Ostriker 1983; Syer et al. 1991; Artymowicz et al. 1993). When the disc forms, about half of the initial of the stellar BH population will be in retrograde orbit if the inner cluster has low angular momentum (Secunda et al. 2021). Nasim et al. (2023) study the capture of low-mass BHs ($q \lesssim 10^{-4}$; q is defined as the ratio between the mass of the satellite BH and that of the central supermassive BH, often abbreviated as SMBH) by the accretion disc. They find that those captured BHs with an inclination larger than a critical value ($i \sim 113^\circ$) increase its inclination until the angular momentum of the BH becomes counteraligned with the angular momentum of the disc (this situation corresponds to $i \sim 180^\circ$).

Intermediate-mass¹ black holes (IMBHs) can also be deposited into the galaxy nuclei and form a binary system with the central SMBH (e.g., Portegies Zwart & McMillan 2002; Volonteri et al. 2003; Portegies Zwart et al. 2006; Bellovary et al. 2010; McKernan et al. 2012; Mastrobuono-Battisti et al. 2014; Yang et al. 2019a,b; Secunda et al. 2020; Szölgén et al. 2021; Di Matteo et al. 2023; Peng

& Chen 2023). After the binary has formed, later accretion event can rejuvenate the accretion disc with gas having uncorrelated angular momentum (e.g., Nixon et al. 2011; Imanishi et al. 2018; Impellizzeri et al. 2019). Nixon et al. (2011) show that the counteralignment occurs if the inclination obeys the condition $\cos i < -J_d/(2J_b)$, where J_d and J_b are the angular momentum of the disc and the binary, respectively. Interestingly, they argue that the orbital shrinking of the binary is more efficient in a retrograde disc.

The interaction between the accretion disc and an orbiter in a (coplanar) retrograde orbit has been studied by several authors (McKernan et al. 2014; Ivanov et al. 2015; Sánchez-Salcedo et al. 2018; Sánchez-Salcedo 2020; Secunda et al. 2021). Retrograde BHs embedded in accretion discs can migrate toward the central SMBH and may eventually merge with it. Ivanov et al. (2015) employ both semi-analytical axisymmetric models and 2D simulations to estimate the torque acting on a retrograde satellite BH with $q \lesssim 0.02$. Sánchez-Salcedo et al. (2018) argue that density waves excited at distances $\lesssim H$, where H is the scaleheight of the disc, can contribute significantly to the torque. The orbital evolution of low-mass retrograde perturbers with eccentricities between 0 and 0.6 was studied numerically in Sánchez-Salcedo (2020).

When the satellite is sufficiently massive, it can open a gap in the surface density of the disc. Ivanov et al. (2015) also develop a criterion for the formation of a gap, and compare the radial gap profiles using axisymmetric models with those obtained in the simulations.

Retrograde discs can be also found in Be/X-ray binaries. Overton et al. (2024) investigate the interaction between the circumprimary

* E-mail: jsanchez@astro.unam.mx

¹ IMBHs are defined as those with masses between 60 and $10^5 M_\odot$.

disc (around the Be star) and the companion, finding that the disc can become unstable to tilt perturbations near the companion's orbital radius.

In this paper, we revisit the criteria for gap formation and investigate the structure of gaps created by embedded non-accreting retrograde perturbers with $q \approx 0.005 - 0.015$, on fixed circular orbits, using two-dimensional (2D) and three-dimensional (3D) simulations. Notably, we find that the perturber does not generally reside at the bottom of the gap but is instead located near its inner wall. Furthermore, we quantify the eccentricity of the gap, as an eccentric rather than circular gap could allow the perturber to intersect it at certain points along its orbit. This interaction is expected to enhance the BH mass accretion rate. We also examine the sensitivity of the results to the inner boundary conditions (IBCs). Additionally, we present some simulations where the perturber is allowed to migrate.

The paper is organized as follows. In Section 2 we provide the theoretical context and present some open issues about the interaction of a retrograde satellite embedded in the midplane of a gas disc. Section 3 describes the set-up and numerical aspects of the simulations. Section 4 provides the outcomes of our 2D simulations. In Section 5, we discuss the results of a 3D simulation. Finally, in Section 6, we present our main conclusions.

2 THEORETICAL CONTEXT AND OUTSTANDING QUESTIONS

We consider a thin accretion disc around a central object with mass M_\bullet . Initially the disc is axisymmetric with surface density $\Sigma(r) \propto r^{-p}$ and gas pressure scale height $H(r)$. The unperturbed accretion disc has aspect ratio $h(r)$ and Shakura-Sunyaev viscosity parameter $\alpha(r)$. The gas rotates at a velocity $\sim \Omega_K r$ (neglecting the gradient pressure), where $\Omega_K(r)$ is the Keplerian frequency. The sound speed of the unperturbed disc is $c_s(r) = \Omega_K H(r)$.

The disc aspect ratio and the α parameter in the accretion discs around SMBHs are rather uncertain. Krolik (1999) estimates $h \approx 0.01$ from radio-continuum emission. On the other hand, models predict that the aspect ratio of AGN accretion discs can vary by orders of magnitude with radial distance r . According to the model of Sirko & Goodman (2003), h reaches a minimum value of 0.01 at $r \approx 10^3 R_S$, where R_S is the Schwarzschild radius. It then increases up to $h = 0.1$ at both $r \approx 10 R_S$ and $r = 10^5 R_S$. Meanwhile, the model of Thompson et al. (2005) indicates that h could be as small as 10^{-3} . Regarding the Shakura-Sunyaev α -parameter, simulations of accretion discs suggest that it may range between 10^{-3} and 10^{-1} (Davis et al. 2010).

We suppose that a gravitational body (representing the satellite or perturber), whose gravitational potential is

$$\Phi_p(\mathbf{r}, t) = -\frac{GM_p}{\sqrt{(\mathbf{r} - \mathbf{r}_p)^2 + R_{\text{soft}}^2}}, \quad (1)$$

is rotating in circular retrograde orbit in the midplane of the disc. Here M_p and $\mathbf{r}_p(t)$ are, respectively, the mass and position vector of the perturber, and R_{soft} is a softening radius. In this study, we focus on the gravitational interaction between the disc and the perturber, while neglecting gas accretion onto the latter.

The relative velocity of the perturber with respect to the local gas is $2\Omega_p r_p$, as it moves in a retrograde circular orbit, where $\Omega_p \equiv \Omega_K(r_p)$. Assuming the sound speed of the disc gas is constant over time (i.e. a locally isothermal disc), the Mach number of the perturber, \mathcal{M} , is expressed as $2\Omega_p r_p / c_s = 2/h_p$, where h_p denotes

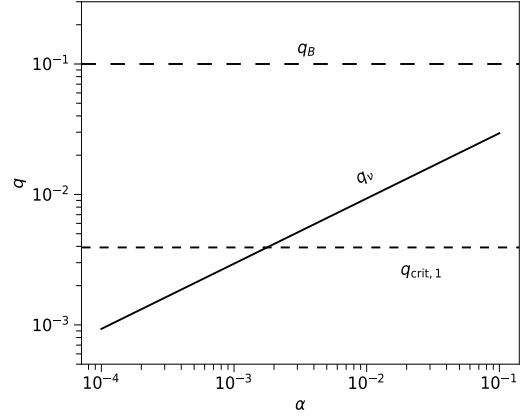


Figure 1. q_v (solid line), q_B (long dashed line) and $q_{\text{crit},1}$ (short dashed line), as a function of α , in a disc with $h = 0.05$ and a perturber with a softening parameter $\mathcal{E} = 0.6$.

the disc aspect ratio at the perturber's location. Consequently, \mathcal{M} is significantly large; for instance, $\mathcal{M} = 40$ when $h_p = 0.05$.

2.1 Condition for opening a gap

We expect that if the accretion radius of the satellite BH, $R_{\text{acc}} = 2GM_p / (2\Omega_p r_p)^2 = qr_p/2$, is comparable to or larger than the disc scale height H , the satellite BH will have a strong impact on the structure of the disc, likely opening a deep gap. This strong shock condition occurs when $q \gtrsim q_B \equiv 2h$. However, it is important to note that the corresponding strong shock condition in the prograde case is not required to open a gap (e.g., Duffell & MacFadyen 2013; Fung et al. 2014; Kanagawa et al. 2015). Thus, this condition should be understood as sufficient but not necessary.

In the following, we infer the condition for the gap not to be refilled by viscosity (or viscous condition), in the retrograde case. The viscous torque in the accretion disc without the perturber is $3\pi r^2 \nu \Sigma_{\text{un}} \Omega_K$, where Σ_{un} is the unperturbed surface density of the disc. Now suppose that the accretion radius of the perturber $R_{\text{acc}} = qr_p/2$ is smaller than R_{soft} . In that case and following the same approximation as in the prograde case (e.g., Goodman & Rafikov 2001; Fung et al. 2014; Duffell 2015), we assume that the excitation of the wake can be calculated in linear theory. In Appendix A, we briefly compile the formula for the torque in linear theory. Hence, we will assume the torque excited in the disc is described by Equations (A3) and (A4), with the unperturbed surface density, $\Sigma_{\text{un},p}$, replaced by the local surface density, Σ_p , once the gap has been carved in the disc. The viscous condition is

$$3\pi r_p^2 \nu \Sigma_{\text{un},p} \Omega_p \leq \frac{\pi \lambda_{\mathcal{E}} q^2 \Sigma_p \Omega_p^2 r_p^5}{4 R_{\text{soft}}}, \quad (2)$$

or

$$q^2 \geq q_v^2 \equiv 12 \left(\frac{h_p \mathcal{E}}{\lambda_{\mathcal{E}}} \right) \left(\frac{\nu}{\Omega_p r_p^2} \right) \left(\frac{\Sigma_{\text{un},p}}{\Sigma_p} \right), \quad (3)$$

where $\mathcal{E} \equiv R_{\text{soft}}/H$. If we demand that the minimum depth to have a gap is $\Sigma_p \lesssim 0.2 \Sigma_{\text{un},p}$ then

$$q_v^2 \equiv 60 \left(\frac{h_p \mathcal{E}}{\lambda_{\mathcal{E}}} \right) \left(\frac{\nu}{\Omega_p r_p^2} \right). \quad (4)$$

Table 1. Parameters of the 2D models. A gap is deep if $\langle \Sigma \rangle_{\text{gap}} \leq \Sigma_{\text{un},p}/4$.

Simulations with $h = 0.05$					
#	q	ν_{-5}	\mathcal{E}	q/q_ν	Comments
1	0.005	1	0.6	0.85	No deep gap
2	0.005	4	0.3	0.77	No deep gap
2B	0.005	4	0.6	0.55	No gap
3	0.01	1/4	0.6	3.39	Deep gap
4	0.01	1	0.6	1.70	Deep gap
5	0.01	4	0.6	0.85	Deep gap
6	0.015	1	0.6	2.54	Deep gap
Simulation with $h = 0.025$					
7	0.005	1	0.6	1.20	Deep gap
Simulation with $h = 0.1$					
8	0.015	1	0.6	1.80	Deep gap

In terms of the Shakura-Sunyaev viscosity parameter α

$$q_\nu^2 = \frac{60\mathcal{E}\alpha h_p^3}{\lambda_{\mathcal{E}}}. \quad (5)$$

Ivanov et al. (2015) propose a different gap-opening condition by requiring some level of non-linearity in the interaction between the perturber and the disc. They argue that the sound radius $r_{c_s} \equiv qr_p/h_p$ should be larger than the most long wavelength of the waves excited by the perturber and obtain that a retrograde perturber opens a gap if $q > q_{\text{crit},1} \equiv 1.57h_p^2$.

Figure 1 compares q_B , q_ν and $q_{\text{crit},1}$ for $\mathcal{E} = 0.6$ and $h_p = 0.05$. For $\alpha \simeq 2 \times 10^{-3}$ (or, equivalently, $\nu \simeq 0.5 \times 10^{-5} \Omega_p r_p^2$), we obtain $q_\nu \simeq q_{\text{crit},1} \simeq 4 \times 10^{-3}$. However, for values of α significantly larger (smaller) than 2×10^{-3} , the viscous condition predicts that a higher (lower) mass ratio is required to open a gap. In Section 4.3, we use 2D simulations to discern whether q_ν or $q_{\text{crit},1}$ is a more reliable predictor for gap formation.

Mass accretion onto the perturber could deepen the gap. However, the simulations by Ivanov et al. (2015) indicate that gas depletion due to accretion has little impact on the azimuthally-averaged surface density profile of the disc.

2.2 Does the disc reach a steady state?

In this subsection, we explore whether a steady-state solution exists for a retrograde perturber embedded in the disc. To do so, we adopt the approach of Duffell (2015), who analyzed the structure of the gap opened by a prograde perturber in the quasi-linear steady-state regime. For a retrograde perturber, the quasi-linear condition requires that R_{soft} be larger than several R_{acc} . Under these conditions, the perturber excites linear waves that carry (negative) angular momentum. When these waves become nonlinear as they propagate through the disc, they deposit the angular momentum in the disc, changing its surface density.

If a steady state solution exists, the mass flow rate through the disc \dot{M} , and the angular momentum flow F_J , should be constant with r . Hence

$$\dot{M} = -2\pi r \Sigma \nu_r = \text{const} \quad (6)$$

and

$$F_J = -\dot{M} r^2 \Omega_K + 3\pi \Sigma \nu r^2 \Omega_K + \Phi_w(r) = \text{const}, \quad (7)$$

where $\Phi_w(r)$ is the angular momentum flux transported by the waves excited by the perturber. We consider the solution $F_J = 0$, which implies

$$-\dot{M} r^2 \Omega_K + 3\pi \Sigma \nu r^2 \Omega_K + \Phi_w(r) = 0. \quad (8)$$

In the absence of the perturber ($\Phi_w = 0$), the equation above implies $\dot{M} = 3\pi \nu \Sigma_{\text{un}}(r)$. This mass flow is expected to be maintained in the presence of the perturber; Equation (8) transforms into:

$$-3\pi \nu \Sigma_{\text{un}} r^2 \Omega_K + 3\pi \Sigma \nu r^2 \Omega_K + \Phi_w(r) = 0. \quad (9)$$

Using Equation (A3), we estimate the angular momentum flux $\Phi_w(r)$ at $r > r_p$ and at $r < r_p$, denoted by Φ_w^+ and Φ_w^- , respectively, as

$$\Phi_w^\pm(r) \simeq \mp \frac{1}{2} \lambda_{\mathcal{E}} \Gamma_0 f(r), \quad (10)$$

where $f(r) > 0$ is a radial function to be specified. If we assume that the excitation torque occurs at a neighbourhood of the perturber, the function $f(r)$ has its maximum at $r = r_p$ and satisfies that $f(r_p) = 1$. Evaluating Equation (9) at $r = r_p$, we obtain

$$\frac{\Sigma_p^\pm}{\Sigma_{\text{un},p}} = \left(1 \mp \frac{\lambda_{\mathcal{E}} q^2 \Omega_p r_p^3}{24 \nu R_{\text{soft}}} \right)^{-1} = \left(1 \mp \frac{5q^2}{2q_\nu^2} \right)^{-1}. \quad (11)$$

In the last equality we have used Eq. (4). This solution is physically unacceptable because, aside from the surface density jump at $r = r_p$, Σ_p^+ becomes negative for $q > \sqrt{2/5} q_\nu$. Therefore, no global steady state exists. Nor does a steady state exist at $r > r_p$, assuming, as we did, that the excitation of the waves occurs in a small region around $r = r_p$. This indicates that the problem is time-dependent, and the long-term solution may depend on the chosen boundary conditions (BCs).

3 HYDRODYNAMICAL SIMULATIONS: CODE AND SETUP

We simulate the evolution of a gaseous disc using the publicly available code FARGO3D (Benítez-Llambay & Masset 2016; Benítez-Llambay et al. 2019) in polar coordinates (r, ϕ) for the 2D simulations and spherical coordinates (r, θ, ϕ) for the 3D simulations. We use a frame where the central mass M_\bullet is at rest at the origin. Initially the disc is axisymmetric with surface density $\Sigma_{\text{un}}(r) = \Sigma_0(r/R_0)^{-1/2}$ and aspect ratio h constant over radius. The evolution of the disc is locally isothermal, that is, the sound speed $c_s(r)$ is constant over time. We also include a kinematic viscosity ν constant over the domain.

At $t = 0$, we insert the perturber on a retrograde circular orbit with radius $r_p = 1$. Unless otherwise stated, the orbit is fixed to be circular. The total gravitational potential is given by

$$\Phi(\mathbf{r}) = -\frac{GM_\bullet}{r} + \Phi_p(\mathbf{r}) + \Phi_I(\mathbf{r}), \quad (12)$$

where $\Phi_p(\mathbf{r})$ is the potential created by the perturber, as given in Eq. (1), and $\Phi_I(\mathbf{r})$ is the indirect term due to the shift of the barycentre in the presence of the perturber

$$\Phi_I(\mathbf{r}) = \frac{GM_p}{r_p^3} \mathbf{r} \cdot \mathbf{r}_p. \quad (13)$$

We include neither mass accretion by the perturber, nor the gas self-gravity, nor the indirect term due to the acceleration felt by the central body from the disc gas.

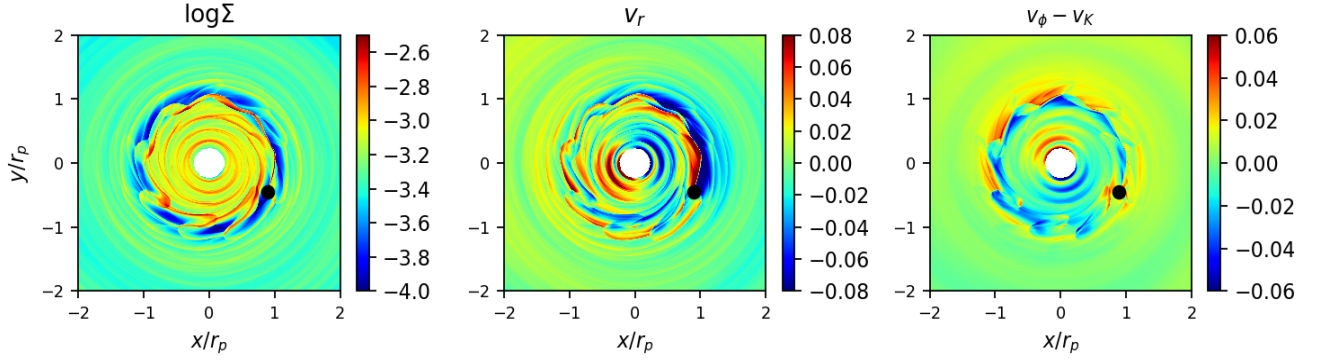


Figure 2. Colour maps of the surface density (left panel), radial velocity (centre) and $v_\phi - v_K$ (right panel; where v_K represents the Keplerian velocity) in 2D simulations after 15 perturber’s orbital periods for model 4 ($q = 0.01$ and $\nu_{-5} = 1$). The perturber’s position is indicated with a black dot. It moves clockwise, whereas the disc rotates counterclockwise.

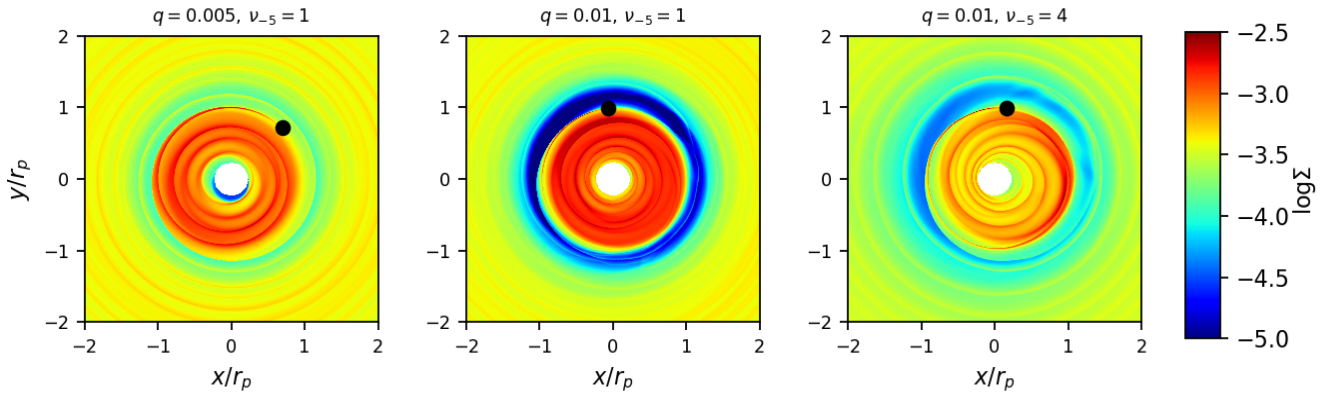


Figure 3. Colour maps of the surface density in 2D simulations at 750 orbits for models 1, 4 and 5 (from left to right). The body moves clockwise, whereas the disc rotates counterclockwise.

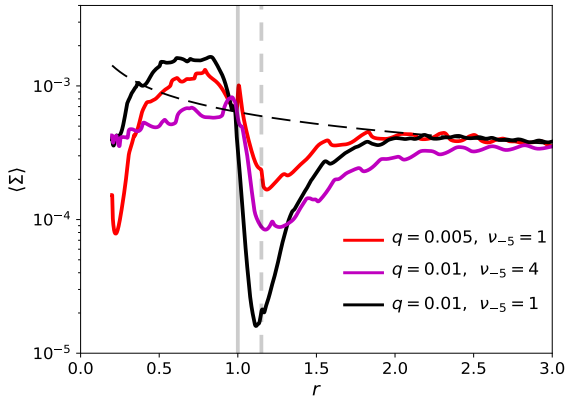


Figure 4. Azimuthally averaged surface density for the three snapshots shown in Figure 3. The long-dashed curve represents the initial surface density, while the vertical lines indicate $r = 1$ (solid) and $r = 1.15$ (dashed) for reference.

4 2D SIMULATIONS

In all our 2D simulations, the inner and outer boundaries are set at $r = 0.2$ and $r = 4$, respectively. We use a grid with 1200 cells in both

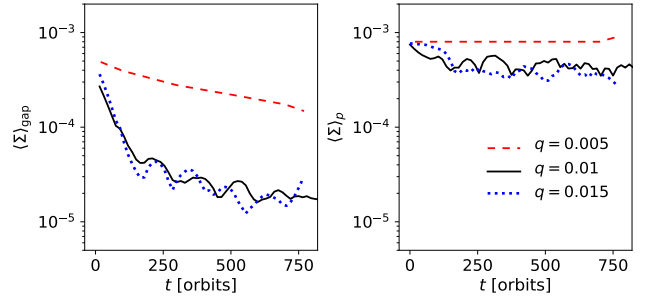


Figure 5. $\langle \Sigma \rangle_{\text{gap}}$ (left column) and $\langle \Sigma \rangle_p$ (right column) for $\nu_{-5} = 1$, and varying q . To avoid cluttering the figure, the values are time averaged over one orbital revolution and taken regularly every 15 orbits.

the radial and azimuthal directions. The radial grid is logarithmic. We apply damping conditions (de Val-Borro et al. 2006) in the outer boundary to prevent reflections of density waves. At the inner edge, we use outflow BCs, that is, we allow mass outflow through the inner boundary (but not mass inflow is permitted)². However, we explore

² With the exception of model 8, where damping IBCs are applied to mitigate the excessive depletion of material in the inner disc caused by outflow IBCs.

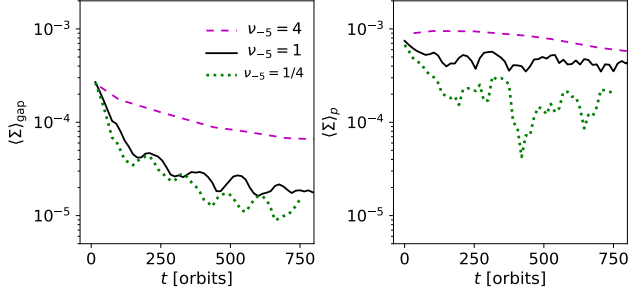


Figure 6. $\langle \Sigma \rangle_{\text{gap}}$ (left column) and $\langle \Sigma \rangle_P$ (right column) for $q = 0.01$ and different viscosities. As in Fig. 5, the values were taken at 15-orbit intervals and time averaged over one perturber’s orbit.

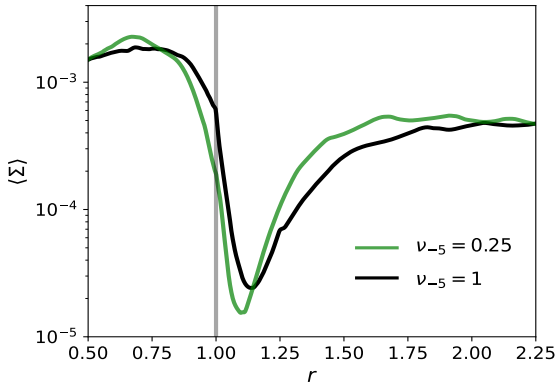


Figure 7. $\langle \Sigma \rangle$, averaged over 100 orbits (from 650 to 750 orbits), for $q = 0.01$ and two values of the viscosity ν (models 3 and 4). The vertical line indicates the position of the perturber.

the impact of using other IBCs (damping and rigid BCs) in Section 4.6.

We consider three values for the perturber-to-central mass ratio: $q = 0.005, 0.01$ and 0.015 ; and three values for the disc viscosity: $\nu_{-5} = 0.25, 1$ and 4 , where $\nu_{-5} \equiv \nu / (10^{-5} \Omega_p r_p^2)$. In most simulations, h is set to 0.05 , and the softening radius of the perturber’s gravitational potential is taken as $R_{\text{soft}} = 0.6H$ (corresponding to $\mathcal{E} = 0.6$). Nevertheless, given the significant variation of h with r expected in AGN accretion discs (see Section 2), we have also considered other values of h . A summary of the models is given in Table 1.

4.1 Azimuthally averaged surface density

At early stages, the flow pattern is far from axisymmetric (see Fig. 2). The radial velocity map clearly reveals the gravitational deflection of streamlines behind the perturber. Even as early as $t = 15$ perturber’s orbital periods, the gas ahead of the perturber is highly disturbed, exhibiting alternating overdense and underdense regions. Within $r < 0.6r_p$, blue and red arcs are visible in both v_r and $v_\phi - v_K$ (here v_K is the Keplerian velocity), indicating that the disc eccentricity is being excited. The behaviour in this early phase of evolution differs from the prograde case, where gaps form smoothly in viscous discs (e.g., Kley 1999).

Figure 3 shows the disc surface density for models 1, 4 and 5, after

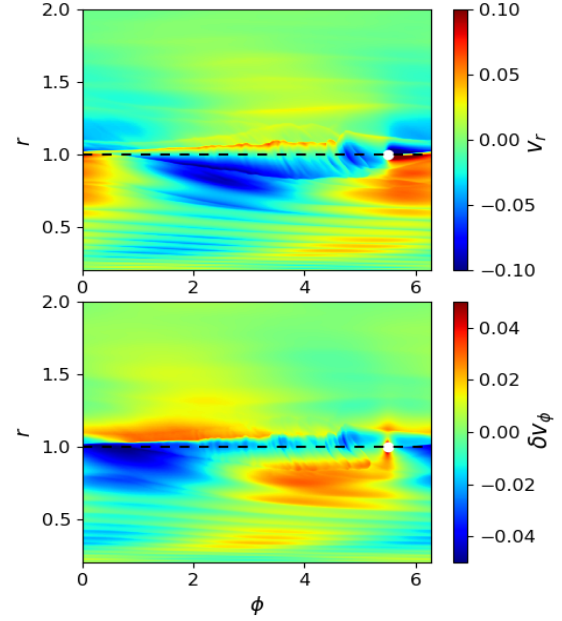


Figure 8. Radial velocity (top panel) and azimuthal velocity perturbations $v_\phi - v_K$ (bottom panel) for model 7 after 50 orbits. The white dot marks the position of the perturber, which moves from right to left. The dashed black line delineates the boundary between the inner and the outer disc.

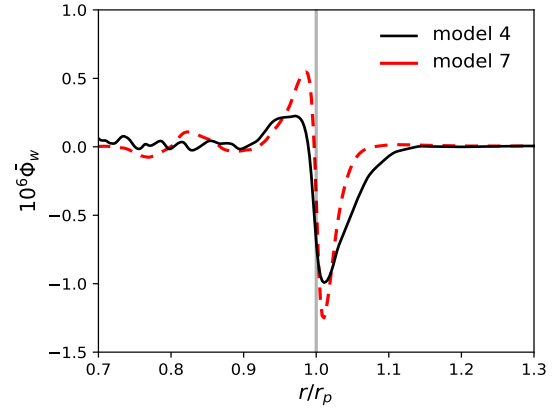


Figure 9. Angular momentum flux carried by propagating density disturbances, Φ_w (see Eq. 14), at $t = 750$ orbits.

750 orbits. In all three cases, the perturber is situated in the edge of the gap. This feature is clearly seen in the azimuthal-averaged surface density profile, which we denote as $\langle \Sigma \rangle$ (see Figure 4). For $q = 0.01$ and $\nu_{-5} = 1$, the bottom of the gap is located at $r \simeq 1.15$. In terms of H , it is radially shifted outward by a distance $3H$ from the perturber’s orbital radius. As a consequence, the azimuthally-averaged surface density at $r = r_p$, $\langle \Sigma \rangle_P$, is about 20 times larger than $\langle \Sigma \rangle_{\text{gap}}$, the azimuthally averaged surface density at the bottom of the gap. Indeed, $\langle \Sigma \rangle_P \simeq \Sigma_{\text{un},P} \equiv \Sigma_{\text{un}}(r_p)$. This is in contrast with the gap opened by a prograde perturber, where the perturber is located at gap’s bottom.

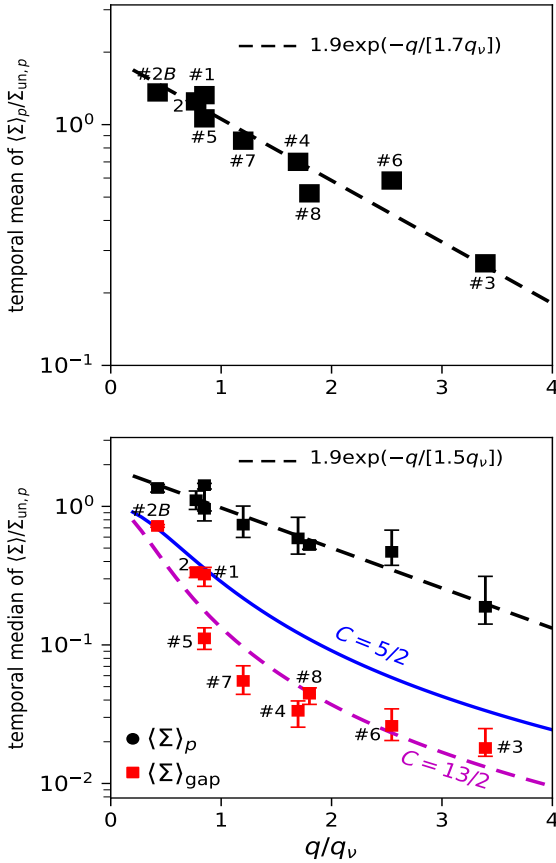


Figure 10. Top panel: Temporal mean value of $\langle \Sigma \rangle_p$, normalized to $\Sigma_{un,p}$, for the models given in Table 1. The dashed black line represents the function $\langle \Sigma \rangle_p / \Sigma_{un,p} = 1.9 \exp(-q/[1.9q_v])$. Bottom panel: Temporal median values of $\langle \Sigma \rangle_p$ (black dots) and $\langle \Sigma \rangle_{gap}$ (red squares), normalized to $\Sigma_{un,p}$, for the same models. The error bars in the bottom panel indicate the 16th and 84th percentile. The mean and median values were taken between 500 to 750 orbits. The blue and magenta curves represent the simple formula given in Equation (15) with $C = 5/2$ and $C = 13/2$, respectively. The dashed black line in the bottom panel represents the function $\langle \Sigma \rangle_p / \Sigma_{un,p} = 1.9 \exp(-q/[1.6q_v])$.

Figure 5 shows $\langle \Sigma \rangle_{gap}$ and $\langle \Sigma \rangle_p$, as a function of time, for $\nu_{-5} = 1$ and three different values of q . The notorious difference between the values of $\langle \Sigma \rangle_{gap}$ and $\langle \Sigma \rangle_p$ reflects the fact that the radius of the gap’s minimum does not coincide with the perturber’s orbital radius. $\langle \Sigma \rangle_{gap}$ presents a decreasing trend with time. It is noteworthy that $\langle \Sigma \rangle_{gap}$ decreases a factor of ~ 10 as q increases from 0.005 to 0.01, but shows only a slight variation when q changes from 0.01 to 0.015.

For $q = 0.01 - 0.015$, $\langle \Sigma \rangle_p$ presents temporal variations about a mean value of $\sim 4 \times 10^{-4}$, which is only a factor 2/3 smaller than its value at $t = 0$.

Figure 6 shows $\langle \Sigma \rangle_{gap}$ and $\langle \Sigma \rangle_p$ for $q = 0.01$ and different disc viscosities. It is clear that the gap is shallower for the highest value of the viscosity ($\nu_{-5} = 4$). Interestingly, $\langle \Sigma \rangle_p$ becomes smaller and exhibits larger temporal variations as viscosity decreases. One could think that $\langle \Sigma \rangle_p$ would decrease in discs with low viscosity due to

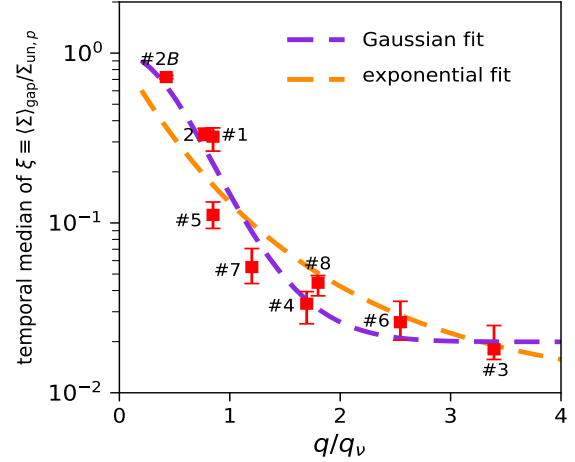


Figure 11. Other fits to the temporal median values of $\xi \equiv \langle \Sigma \rangle_{gap} / \Sigma_{un,p}$ (red squares). The violet line represents the function $\log \xi = 1.7(\exp\{-0.67[q/q_v]^2\} - 1)$, whereas the orange represents the function $\log \xi = 2(\exp\{-0.58[q/q_v]\} - 1)$.

the widening of the gap. However, our simulations indicate that, in contrast to the prograde case (e.g., Kanagawa et al. 2016), the gap width in the retrograde configuration increases with viscosity. The value $\langle \Sigma \rangle_p$ is smaller for $\nu_{-5} = 0.25$, because the radial shift between the gap minimum and the perturber’s orbital radius decreases for lower values of ν_{-5} (see Figure 7).

The indirect term Φ_I takes into account the reflex motion of the central star around the centre of mass. We have explored the role of the indirect term by comparing the azimuthally averaged surface density $\langle \Sigma \rangle$, $\langle \Sigma \rangle_{gap}(t)$ and $\langle \Sigma \rangle_p(t)$, for a simulation with and without the indirect term Φ_I in the gravitational potential. We found that these quantities are not affected, in a statistical sense, by the indirect term.

4.2 Why is the perturber offset from the minimum of the gap?

The result that a non-migrating perturber does not lie at the bottom but at edge of the gap is a bit unexpected. In fact, we have applied an imposed (external) torque to the disc (without any gravitational perturber), $|\Lambda_{imp}(r)| \propto \exp(-\lambda[r - r_0]^2)$, and confirmed that the resulting gap has its minimum at $r = r_0$.

The simplest hypothesis for the radial shift between the gap and the perturber is the distinct dynamical responses of the inner ($r < r_p$) and outer $r > r_p$) disc regions (see Figures 2 and 8). The asymmetry between the inner and outer parts of the disc arises in the non-linear regime as soon as the perturber reaches its own wake. This asymmetrical behaviour likely results in a reduction of the deposition of (negative) angular momentum within the inner disc.

As an indication of this potential reduction in angular momentum deposition within the inner disc, we have computed

$$\Phi_w(r) = r^2 \int_0^{2\pi} (v_\phi - \langle v_\phi \rangle)(v_r - \langle v_r \rangle) \Sigma d\phi, \quad (14)$$

which serves as a proxy for the angular momentum flux carried by the propagating density disturbances. Figure 9 presents $\Phi_w(r)$, where the overbar denotes an average over one orbit of the perturber, calculated after it has completed 750 orbits, for models 4 and 7. In both cases, Φ_w is far from being antisymmetric with respect to $r = r_p$. For both models, density waves excited in the outer disc transport

(negative) angular momentum outward. Interestingly, although waves are also excited in the inner disc, they carry significantly less angular momentum over one perturber's orbital period, particularly in model 4.

Therefore, we attribute the shift between the perturber and the centre of the gap to the unequal transfer of angular momentum between the perturber and the inner disc compared to the perturber and the outer disc. We further suggest that models excluding this effect (e.g. Ivanov et al. 2015) are likely to predict gaps that are excessively deep.

4.3 Gap formation criterion

In this section, we study how $\langle \Sigma \rangle_{\text{gap}}$ and $\langle \Sigma \rangle_p$ scale with the parameter q/q_v . The upper panel of Figure 10 shows the time- and azimuthally-averaged surface density at $r = r_p$, in units of $\Sigma_{\text{un},p}$, as a function of q/q_v , for the simulations in Table 1. The average over time was done from 500 to 750 orbits. The lower panel shows the median values of $\langle \Sigma \rangle_p$ and $\langle \Sigma \rangle_{\text{gap}}$ in the same time series. All these quantities decay with q/q_v (albeit with some scatter). The functional dependence can be fitted reasonably well with

$$\frac{\langle \Sigma \rangle}{\Sigma_{\text{un},p}} = \left(1 + \frac{Cq^2}{q_v^2} \right)^{-1}. \quad (15)$$

For the mean and median values of $\langle \Sigma \rangle_p$, we find $C = 0.59$ and $C = 2/3$, respectively. For the median value of $\langle \Sigma \rangle_{\text{gap}}$, $C \approx 13/2$. Albeit with some scatter, $(q/q_v)^2$ can be considered an ordering parameter. The coefficient of $C = 5/2$ predicted in Section 2.2 overestimates the value of $\langle \Sigma \rangle_{\text{gap}}$ and underestimates the value of $\langle \Sigma \rangle_p$.

We explored whether alternative functional forms provide a better fit than Equation (15). Define $\xi \equiv \langle \Sigma \rangle_{\text{gap}} / \Sigma_{\text{un},p}$. Figure 11 reveals that the exponential dependence of $\log \xi$ on q/q_v provides a comparable fit to Eq. (15), whereas the Gaussian fit yields a slightly closer agreement. However, the flat behaviour of $\log \xi$ at large q/q_v values predicted by the Gaussian curve appears to be physically unrealistic.

Note that $\langle \Sigma \rangle_p \geq \Sigma_{\text{un},p}$ for $q \leq q_v$. In the particular case of model 1, the density enhancement in the wake behind the perturber overbalances the density reduction due to the angular momentum transfer between the perturber and the disc (see Fig. 4). On the other hand, it can be seen that $q \geq 1.2q_v$ is a sufficient (but not necessary) condition for the formation of a deep gap.

In all the models from 1 to 6 in Table 1, we have taken $h = 0.05$. Consequently, $q_{\text{crit},1} = 0.004$ for these models. Since all the simulations in Figure 10 satisfy $q > q_{\text{crit},1}$ (see Table 1), all of them should present a gap according to this criterion. However, in models 1, 2 and 2B, where $q = 0.005$, the perturber cannot open a deep gap.

4.4 The fluctuating flow around the perturber

In Section 4.1, we have shown that the perturber is located in the inner wall of the gap, i.e. in a region with a steep radial density gradient. Therefore, both axisymmetric oscillatory modes and non-axisymmetric radial motions in the disc, if exist, are expected to produce a very fluctuating flow pattern around the body.

In order to quantify this flow variability, we have divided the disc into eight equally-sized azimuth sectors. We denote S1 to the azimuth sector just behind the perturber (it extends in azimuth from $\phi = \phi_p$ to $\phi_p + \pi/4$, where ϕ_p is the perturber's azimuthal angle), whereas S8 is the sector just ahead of the perturber. More specifically, we define the surface density averaged over sector S $_j$ as

$$\langle \Sigma \rangle_{S_j} = \frac{4}{\pi} \int_{\phi_p + (j-1)\beta}^{\phi_p + j\beta} \Sigma(r, \phi, t) d\phi, \quad (16)$$

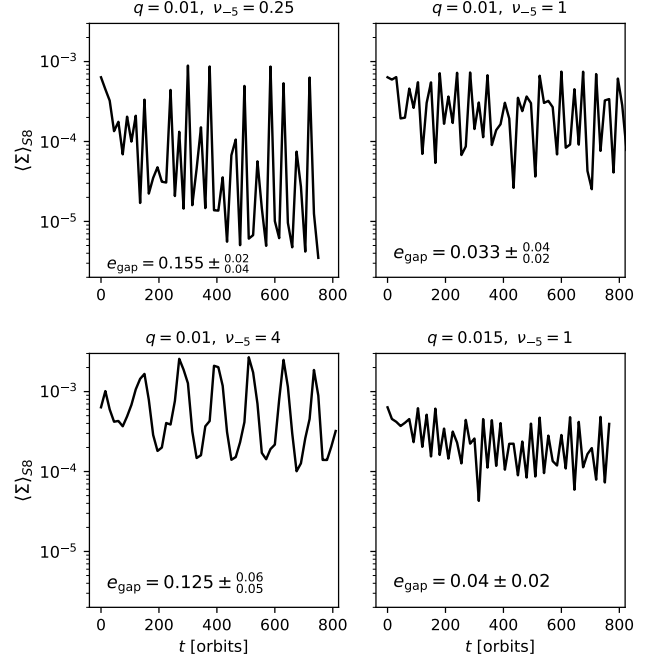


Figure 12. $\langle \Sigma \rangle_{S8}$ at $r = r_p$ as a function of time for runs 3, 4, 5 and 6. To keep the figure uncluttered, the values were taken at 15-orbit intervals. The periodic oscillations of $\langle \Sigma \rangle_{S8}$ in model 5 result from an aliasing effect, as the sampling rate is low compared to the true frequency of the oscillations.

with $\beta = \pi/4$. Since S8 is the sector just at the front of the perturber, the mass accretion rate onto the perturber (if it were an accretor, which is not the case in our simulations) is more directly related to $\langle \Sigma \rangle_{S8}$ at $r = r_p$ than to $\langle \Sigma \rangle_p$.

Figure 12 shows $\langle \Sigma \rangle_{S8}$ at $r = r_p$, taken every 15 orbits, for four representative models. It is apparent that $\langle \Sigma \rangle_{S8}$ at $r = r_p$ is more fluctuating than $\langle \Sigma \rangle_p$ (compare the right-hand panel of Fig. 6 and Fig. 12). This is expected because $\langle \Sigma \rangle_p$ in Figs. 5 and 6 involves an averaging process over one orbit of the perturber. Without this averaging, $\langle \Sigma \rangle_p$ would exhibit variations over one orbital time due to the presence of axisymmetric oscillatory modes in the disc.

For the models under consideration, the temporal mean value of $\langle \Sigma \rangle_p$ is a factor of ~ 1.5 larger than $\langle \Sigma \rangle_{S8}$ at $r = r_p$. The reason is that, unlike $\langle \Sigma \rangle_{S8}$, $\langle \Sigma \rangle_p$ includes the (overdense) wake trailing the perturber.

In the model with $q = 0.01$ and $\nu_{-5} = 1/4$, $\langle \Sigma \rangle_{S8}$ at $r = r_p$ shows the largest variations, spanning approximately two orders of magnitude. Among the four models, the model with $q = 0.015$ displays the smallest variations in $\langle \Sigma \rangle_{S8}$, with a variation factor of ~ 6 , compared to a factor of ~ 15 for the $q = 0.01$ model with the same viscosity.

4.5 Gap and disc eccentricities

Given the strong radial density gradient at the gap's edge, dynamical instabilities, such as the Rayleigh instability, are likely to excite the gap's eccentricity, which may contribute to produce the observed fluctuations in $\langle \Sigma \rangle_{S8}$ at $r = r_p$. Therefore, evaluating the eccentricity of the inner edge of the gap is of particular interest. Furthermore, modelling the interaction with axisymmetric models (as in Section 2) is only justified if the eccentricity of the inner edge of the gap,

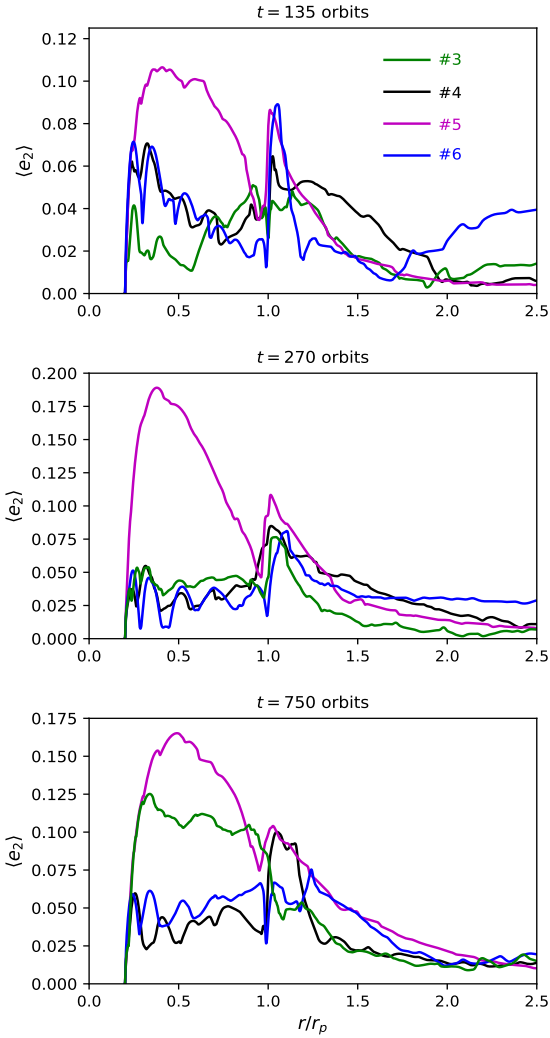


Figure 13. Disc eccentricity, $\langle e_2 \rangle$, at three different times: 135 orbits (upper panel), 270 orbits (central panel) and 750 orbits (lower panel), for models 3, 4, 5 and 6.

e_{gap} , is small enough that $e_{\text{gap}} r_p$ remains less than the width of the gap.

To compute e_{gap} , we follow this procedure. First, we define the edges of the gap using two isocontours corresponding to a surface density of $\Sigma_{\text{un},p}/2$. At a given time t , the inner edge is represented by a polar equation $r(\theta)$. We then search for the value of θ at which r reaches its maximum, denoted as $\theta_{\text{max}}(t)$. The gap eccentricity is calculated using the following formula:

$$e_{\text{gap}}(t) \equiv \frac{r(\theta_{\text{max}}) - r(\theta_{\text{max}} + \pi)}{r(\theta_{\text{max}}) + r(\theta_{\text{max}} + \pi)}. \quad (17)$$

Note that this definition of the gap eccentricity is meaningful only for deep gaps, i.e. those having $\langle \Sigma \rangle_p \leq \Sigma_{\text{un},p}/4$.

The complex interaction between the perturber and the edge of the gap induces temporal variations in e_{gap} . Therefore, in Table 2 and in each panel of Figure 12, we report the median value of e_{gap} along

with the 16th and 84th percentiles, calculated over the time series from 500 to 750 orbits. We see that e_{gap} may acquire large values (~ 0.18) in runs 3 and 5. Nevertheless, the effect of eccentric modes on $\langle \Sigma \rangle_{S8}$ at $r = r_p$ depends not only on e_{gap} but also on the density gradient. For instance, in simulation 5, although e_{gap} is large, the variations in $\langle \Sigma \rangle_{S8}$ remain moderate due to the relatively shallow density radial gradient compared to the other simulations.

In run 4, the gap remains relatively circular. However, as viscosity is either decreased or increased, the gap becomes more eccentric. This unexpected result that e_{gap} is not a monotonic function of viscosity, suggests a spurious excitation of e_{gap} in the inner boundary in run 5. It is therefore important to track the growth of the eccentricity at various distances in the disc.

To do so, we have computed the ‘‘disc eccentricity’’ at different times. Some authors refer to the disc eccentricity as the azimuthally averaged value of e_{disc} , which is defined as

$$e_{\text{disc}}(r, \phi, t) \equiv \sqrt{\left(\frac{v_{\phi}^2}{v_K^2} - 1\right)^2 + \frac{v_r^2 v_{\phi}^2}{v_K^4}}, \quad (18)$$

where $v_K(r) = \sqrt{GM_{\bullet}/r}$ is the Keplerian velocity (Kley & Dirksen 2006; Tanaka et al. 2022). The azimuthal averaged of e_{disc} , $\langle e_{\text{disc}} \rangle$, measures how much a ring of the disc separates from Keplerian rotation. Tanaka et al. (2022) suggest that $e'_2 \equiv |v_r v_{\phi}|/v_K^2$ is a better estimator of how a ring separates from circular rotation. Still, an axisymmetric disc with a radial flow has a non-null e'_2 . Therefore, we expect that $\langle e_2 \rangle$ with

$$e_2 \equiv \frac{|(v_r - \langle v_r \rangle) v_{\phi}|}{v_K^2} \quad (19)$$

is a better proxy of asymmetry.

Figure 13 shows $\langle e_2 \rangle$ versus r , at three different times (at $t = 135, 270$ and 750 orbits), in models 3, 4, 5 and 6. Note that, in general, $\langle e_2 \rangle$ at $r = r_p$ is smaller than e_{gap} . Thus, $\langle e_2 \rangle$ should not be interpreted as the ellipticity of the surface density isocontours, but as a measurement of disc asymmetries. In most of the cases, $\langle e_2 \rangle$ exhibits a local maximum at $r \approx 1.15$, indicating the signature of the wake excited by the perturber. At $t = 750$ orbits, $\langle e_2 \rangle$ at $r = r_p$ lies between 0.04 and 0.1.

In model 5, we observe that $\langle e_2 \rangle$ reaches its peak around $r \approx 0.4 r_p$ in the three panels, suggesting that, at $t = 135$ orbits and beyond, the excitation of the disc eccentricity due to the interaction of wakes with the inner boundary may contribute to enhance the gap eccentricity. In models 4 and 6, the inner computational boundary does not appear to significantly impact the gap eccentricity, at least up to $t = 750$ orbits. Conversely, in model 3, spurious interactions between the wakes and the inner boundary seem to drive an increase in the gap eccentricity beyond ~ 360 orbits.

In summary, from 500 to 750 orbits, $\langle e_2 \rangle$ may be dominated by artificial boundary effects in models 3 and 5. In contrast, the impact of the inner boundary on $\langle e_2 \rangle$ remains small in models 4 and 6, where $\langle e_2 \rangle$ is ~ 0.07 at the 84% of the distribution. In the following subsection, we examine how the structure of the gap changes when other IBCs are applied.

4.6 The impact of the IBCs

In the prograde case, damping BCs, as described in de Val-Borro et al. (2006), are the most commonly applied in both the inner and outer boundaries of the computational domain. Prior to the introduction of damping BCs, some authors implemented outflow IBCs (e.g., Kley

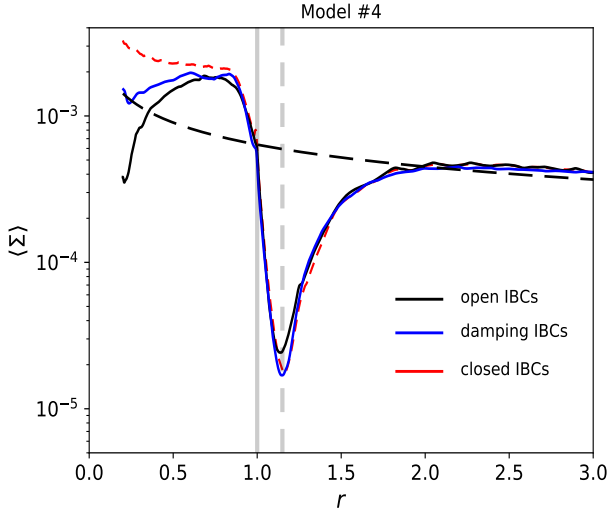


Figure 14. Surface density averaged over both azimuth and time, between 650 and 750 orbits, using different IBCs: outflow (solid line), damping (blue line) and rigid (red line) IBCs. The initial surface density profile is also shown with a long dashed line. The vertical solid grey line indicates $r = 1$ (where the perturber is located) and the dashed grey line indicates $r = 1.15$ (which is approximately the location of the bottom of the gap). In all cases, $q = 0.01$ and $\nu_{-5} = 1$.

Table 2. Median values, 16th, and 84th percentiles of e_{gap} (as given in Eq. 17) over the time series from 500 to 750 orbits for the three types of IBCs in 2D simulations.

#	e_{gap} outflow IBCs	e_{gap} damping IBCs	e_{gap} rigid IBCs
3	$0.155^{+0.02}_{-0.04}$	$0.12^{+0.02}_{-0.04}$	$0.10^{+0.05}_{-0.01}$
4	$0.033^{+0.04}_{-0.02}$	$0.035^{+0.015}_{-0.03}$	$0.043^{+0.01}_{-0.02}$
5	$0.125^{+0.06}_{-0.05}$	$0.135^{+0.04}_{-0.05}$	$0.095^{+0.04}_{-0.02}$
6	0.04 ± 0.02	$0.16^{+0.02}_{-0.03}$	$0.25^{+0.17}_{-0.05}$
7	$0.065^{+0.01}_{-0.03}$	$0.060^{+0.02}_{-0.025}$	$0.065^{+0.02}_{-0.035}$
8	--	$0.027^{+0.035}_{-0.02}$	--

1999; Snellgrove et al. 2001; D’Angelo et al. 2003; Hosseinbor et al. 2007), whereas other authors chose rigid IBCs (e.g., Lubow, Seibert & Artymowicz 1999; Kley et al. 2001; Bate et al. 2003; Nelson & Papaloizou 2003). For times shorter than the viscosity timescale and with boundaries sufficiently distant from the perturber, the torque on a prograde perturber and the gap structure are largely unaffected by the BCs. This is because spiral waves are excited at the Lindblad and corotation resonances, and the torque is dominated by resonances at distances of $\sim h$ from the perturber (Goldreich & Tremaine 1980). Since there are no resonances between the orbiter and the disc in the circular retrograde case, the disc response, and consequently the torque acting on the orbiter, are expected to be more sensitive to the IBC than in the prograde case.

In this subsection, we explore how the results depend on the adopted IBC in 2D simulations. We compare the results using three types of IBCs: outflow, damping and rigid. Figure 14 shows the azimuthally-averaged (and time averaged) surface density for model

4. We see that beyond $r = 0.8r_p$, the radial profiles of $\langle \Sigma \rangle$ are similar for the three IBCs.

Figures 15 and 16 show $\langle \Sigma \rangle_{\text{gap}}$ and $\langle \Sigma \rangle_p$, respectively, as a function of time, for different IBCs. In all the models shown in Fig. 15, $\langle \Sigma \rangle_{\text{gap}}$ exhibits a decreasing trend over time, except for model 6 with rigid IBCs. A comparison of results for outflow and damping IBCs reveals that both predict similar values for $\langle \Sigma \rangle_{\text{gap}}$ and $\langle \Sigma \rangle_p$, except in model 6, where the damping IBC predicts a $\langle \Sigma \rangle_p$ value lower by a factor of 2 (see the fourth panel in Fig. 16).

Figure 17 shows $\langle e_2 \rangle$ at 750 orbits, for the same models as depicted in Figures 15 and 16. Among the three IBCs, model 4 exhibits the lowest eccentricity excitation at $r < r_p$. In model 5, the disc eccentricity exhibits significant excitation at the boundary across all three types of IBCs. In this model, $\langle e_2 \rangle$ at 750 orbits is similar for both outflow and damping IBCs. In model 6, the disc eccentricity is less excited with outflow IBCs, whereas in model 3, outflow IBCs result in the highest $\langle e_2 \rangle$ values at $r < r_p$.

The gap eccentricity, e_{gap} , is also expected to be sensitive to the IBCs. Table 2 provides the median values of e_{gap} over the time series from 500 to 750 orbits for the three different types of IBCs. For model 3, e_{gap} is slightly higher when using outflow IBCs. In model 4, e_{gap} is not very different across the three types of IBCs. In model 5, the lowest e_{gap} is obtained for rigid IBCs, while in model 6, e_{gap} is significantly lower with outflow IBCs. Consequently, no specific IBC minimizes disc eccentricity across all four models.

Fig. 18 shows $\langle \Sigma \rangle_{S8}$ at $r = r_p$ in model 6, using outflow and damping IBCs. The figure clearly demonstrates the sensitivity of $\langle \Sigma \rangle_{S8}$ to e_{gap} . In fact, $\langle \Sigma \rangle_{S8}$ displays greater temporal variations with damping IBCs as e_{gap} is significantly larger under these IBCs.

In the previous and current subsections, we have kept the perturber’s orbit fixed and focused on the disc eccentricity. However, the perturber’s eccentricity can also grow. In Appendix B, we present the radial migration and the evolution of the eccentricity of the perturber when migration is allowed.

5 3D SIMULATION

Our 2D simulations indicate that the satellite is embedded in the inner edge of the gap, a region with a large density gradient. To study the 3D structure of the gap and, in particular, the flow at the edges of the gap, we have performed one 3D simulation with the same parameters of q , ν and \mathcal{E} as in model 4. We simulate only the upper half of the disc. The inner boundary is located at $r = 0.3$, the outer boundary at $r = 3$, and the upper boundary at a latitude angle of 13.75° , which corresponds to $z_{\text{max}} = 4.8H$, where H is the vertical disc scaleheight. The number of cells are $n_r = 276$, $n_\phi = 576$, and $n_\theta = 40$. Since the softening radius R_{soft} is $0.6H_p$, we have 3 zones per R_{soft} in the radial and azimuthal directions, and 5 zones per R_{soft} in the vertical direction. The boundaries are rigid in the inner and outer radii. At the upper cap of the domain, we apply open BCs. As in our 2D simulations, the disc is initialized with a power-law radial profile $\Sigma \propto R^{-0.5}$ and aspect ratio $h = 0.05$.

Figure 19 shows the volume density at the midplane of the disc ($z = 0$) and the surface density (i.e. the vertically integrated volume density) at three different times. We observe that the maps of volume density at $z = 0$ and surface density are highly similar, suggesting that the dynamics of the disc’s bulk mass is largely cylindrical. A very thin tail behind the perturber is visible in the three maps of the volume density at $z = 0$, and it is less pronounced or not visible in the integrated surface density.

After 60 orbits, the gap is still incipient and non-axisymmetric. We

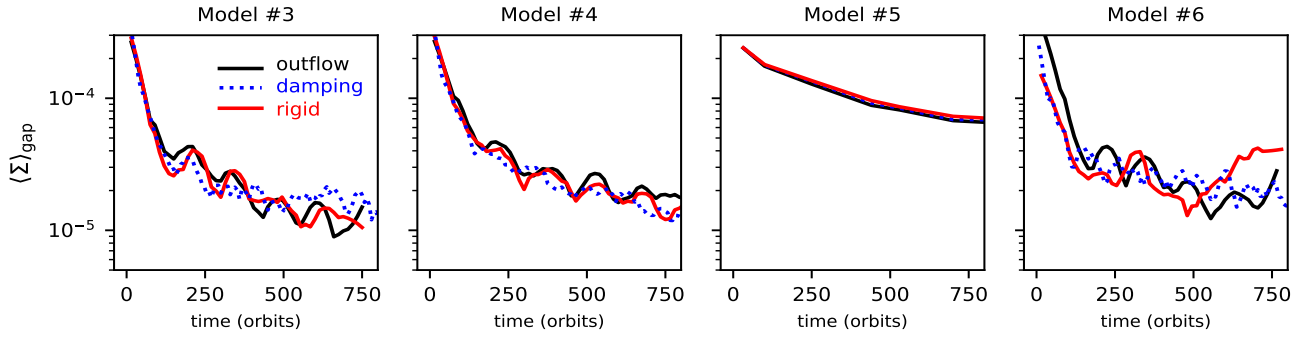


Figure 15. Comparison of $\langle \Sigma \rangle_{\text{gap}}$ for different IBCs: outflow (black lines), damping (blue lines) and rigid (red lines) in models 3, 4, 5 and 6. As in Figures 5 and 6, $\langle \Sigma \rangle_{\text{gap}}$ was computed every 15 orbits of the perturber and time averaged over one orbit.

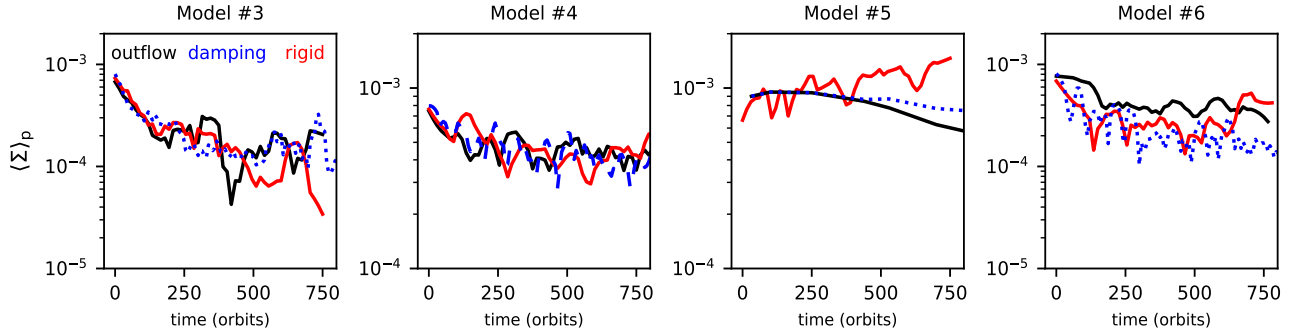


Figure 16. Similar to Figure 15 but for $\langle \Sigma \rangle_p$.

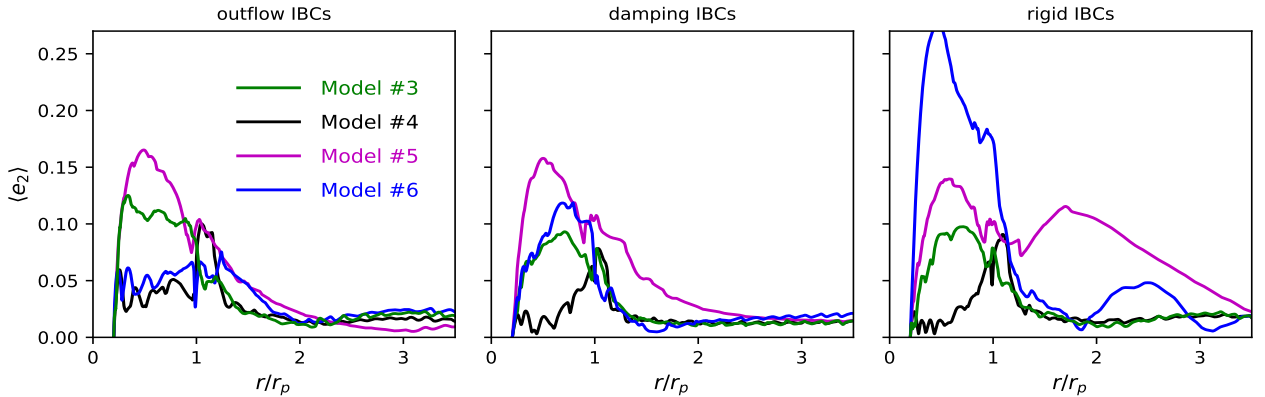


Figure 17. $\langle e_2 \rangle$ at 750 orbits, for outflow (left panel), damping (middle panel) and rigid (right panel) IBCs, for models 3, 4, 5 and 6.

can see some gas plumes in the forming-gap. After 690 orbits, the gap is more deep and becomes more axisymmetric, although some corrugations in the inner edge of the gap are visible. At 1500 orbits, although the gap appears slightly wider, some corrugations along the inner edge are still present. Similar to the 2D simulations, the orbiter is positioned at inner rim of the gap, as observed in both the surface density and volume density maps.

Figures 20 and 21 show the density and velocity vectors along R - z slices, averaged over different sectors (S1, S3, S5 and S7), at $t = 60$ orbits and at $t = 1500$ orbits, respectively. Between $R \simeq 0.9$ and $R = 1.1$, the flow velocity exhibits a notorious vertical component. Additionally, the velocity field varies markedly across

different sectors. For example, in many locations, the velocity arrows in sectors S1 and S5 point in opposite directions. Unlike the prograde case (see Fig. 4 in Fung & Chiang 2016), the gas dynamics at the inner edge differ entirely from those at the outer edge.

Let us first consider the sector S1. Recall that S1 is the sector just behind the perturber. In both Figs. 20 and 21, within the range $0.9 \leq R \leq 1.1$, the velocity is supersonic and the vectors point toward the perturber, creating a region of compression. The velocity in this region is induced by the gravitational pull by the perturber. A tiny density enhancement at $(R, z) = (1, 0)$ associated with the tail excited by the perturbed can be seen in S1 of Fig. 20. After the passage of the perturber, the high pressure generated by the vertical

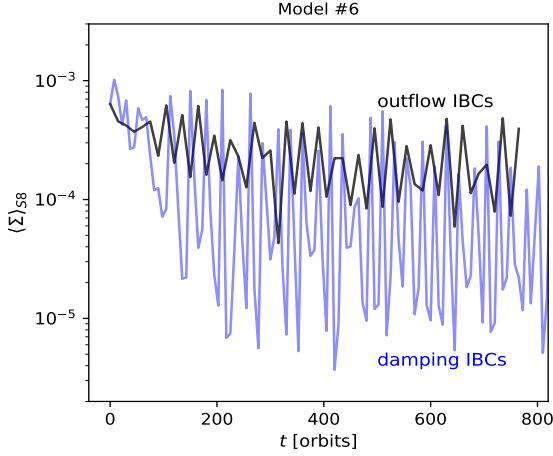


Figure 18. $\langle \Sigma \rangle_{S8}$ at $r = r_p$ as a function of time, using outflow IBCs (black line) and damping IBCs (blue line), in model 6 ($q = 0.015$ and $\nu_{-5} = 1$).

compression drives gas upward in S5 and S7 and, consequently, the inner “wall” of the gap (i.e. the material between $R = 0.8$ and $R \simeq 1$) expands in the vertical direction.

In sectors S1 and S3, the flow within the gap and the outer disc ($R \gtrsim 1.2$) moves radially inward. Along the gap, the flow accelerates until it collides supersonically (with Mach number 3-4) with the inner wall. In contrast, in sectors S5 and S7, the gas in the gap and in the outer disc (at $R > 1.1$) flows radially outwards. This variation in the radial velocity direction across different sectors is attributed to the eccentricity of the outer edge of the gap. As a result of this outward motion, the gap exhibits a marginally greater width in S7 relative to S5.

In Figure 22, we plot $\langle \Sigma \rangle$ at $t = 690$ orbits, for both the 2D and 3D simulations. In the 2D simulation, we used the same domain extension and number of zones in both the radial and azimuthal directions as in the 3D simulation. The gap appears slightly more pronounced in the 2D case. Although the shape of the gap is similar in both simulations, they are slightly offset radially. This radial offset, though small, results in a lower value of $\langle \Sigma \rangle_p$ in the 3D simulation.

For a more quantitative comparison, Figure 23 shows $\langle \Sigma \rangle_{\text{gap}}$, $\langle \Sigma \rangle_p$ and $\langle \Sigma \rangle_{S8}$ at $r = r_p$, versus time. Remarkably, the amplitude of the temporal variations in these three quantities is considerably smaller in the 3D case compared to the 2D case. Beyond 500 orbits, $\langle \Sigma \rangle_{\text{gap}}$ is, on average, a factor of ~ 1.3 smaller in the 2D case compared to the 3D simulation. This result is reasonable to some extent, as the same value of \mathcal{E} is used in both simulations and, therefore, the torque in the 2D simulation is greater at distances $\lesssim H$ from the perturber compared to the 3D simulation. In contrast, the $\langle \Sigma \rangle_p$ values in the 3D simulation are approximately 2.5 times smaller than in the 2D case. As shown in Figure 22, this difference arises from the radial offset in the gap position and a slight change in the slope of the radial density profile at the inner edge of the gap. Interestingly, while $\langle \Sigma \rangle_p$ is a factor of 2.5 smaller in the 3D case compared to the 2D case, the values of $\langle \Sigma \rangle_{S8}$ at $r = r_p$, averaged from 200 to 1100 orbits, are quite similar.

6 SUMMARY AND CONCLUSIONS

The gravitational interaction between a satellite on a fixed circular orbit and a retrograde rotating disc differs fundamentally from the

prograde case. In the prograde scenario, the interaction is governed by Lindblad and corotation resonances, whereas no resonances are present in the retrograde case. The formation and structure of gaps also differs between retrograde and prograde orbiters. To quantify the depth and eccentricity of these gaps, examine the relative position of the perturber with respect to the gap’s minimum, estimate the disc eccentricity and evaluate the influence of the IBCs, we have conducted a number of 2D simulations. These simulations involve a non-accreting perturber with $q = 0.005 - 0.015$ on a retrograde orbit within the midplane of a viscous gas disc (ν_{-5} was varied between 0.25 and 4).

We find that a viscous criterion for gap formation, derived for perturbers in circular orbits (Equation 5), aligns well with simulation results. We have also examined the scaling of gap depth, $\Sigma_{\text{gap}}/\Sigma_{\text{un},p}$ with q/q_v and identified a trend between them, albeit with some scatter.

In contrast to the prograde case, the body does not sit at the gap’s minimum but is located on the inner rim of the gap. As a result, $\langle \Sigma \rangle_p$ can be up to 20 times larger than $\langle \Sigma \rangle_{\text{gap}}$.

The perturber, even when fixed on a circular orbit, drives radial motions in the disc, causing temporal variations in both $\langle \Sigma \rangle_{\text{gap}}$ and $\langle \Sigma \rangle_p$ over an orbital period. In addition, the perturber can excite eccentric modes in the disc. As a consequence, the surface density ahead of the body, $\langle \Sigma \rangle_{S8}$, may be highly fluctuating. However, we have found that the level of disc eccentricity excitation, and thus the amplitude of the fluctuations in $\langle \Sigma \rangle_{S8}$ is sensitive to the IBCs. We have noticed that, over sufficiently long times, the disc eccentricity may be dominated by spurious effects generated at the inner boundary. Special care should be taken with simulations where $q > 0.015$ or $\mathcal{E} \leq 0.3$, as these boundary effects might lead to unrealistic results after a few hundred orbits.

We find that in the freely migrating case, the migration is faster in discs with higher viscosity. The gravitational coupling between the satellite and the disc lead to the excitation of the satellite’s orbital eccentricity up to values comparable to the disc aspect ratio h .

We have also conducted a 3D simulation with $q = 0.01$ and $\nu_{-5} = 1$ to investigate the meridional flow in the disc. Like in the 2D simulations, the perturber is located at the inner edge of the gap. Behind the perturber (in sector S1), the gravitational pull of the perturber compresses the gas flow radially and vertically. This compression accelerates radially along the gap and collides supersonically with the inner edge of the gap. Behind this compression tail (sectors S3 to S7), the gas at the gap’s edge moves upward away from the midplane.

We have compared $\langle \Sigma \rangle_{\text{gap}}$, $\langle \Sigma \rangle_p$ and $\langle \Sigma \rangle_{S8}$ from the 3D simulation to those from the 2D simulation. Our results show that $\langle \Sigma \rangle_{\text{gap}}$ is slightly higher in the 3D simulation, while $\langle \Sigma \rangle_p$ is ~ 2.5 times lower in the 3D simulation. Additionally, the amplitude of the temporal variations in $\langle \Sigma \rangle_{S8}$ is reduced in the 3D compared to the 2D simulation.

More realistic simulations should include the accretion of mass onto the perturber, as in Ivanov et al. (2015). Another limitation of our 3D simulation is that we imposed reflection symmetry between the upper and lower halves of the disc, which may suppress the onset of vertical instabilities. We plan to perform fully 3D simulations to explore whether the tilting instability found by Overton et al. (2024) can also arise in the case of embedded perturbers.

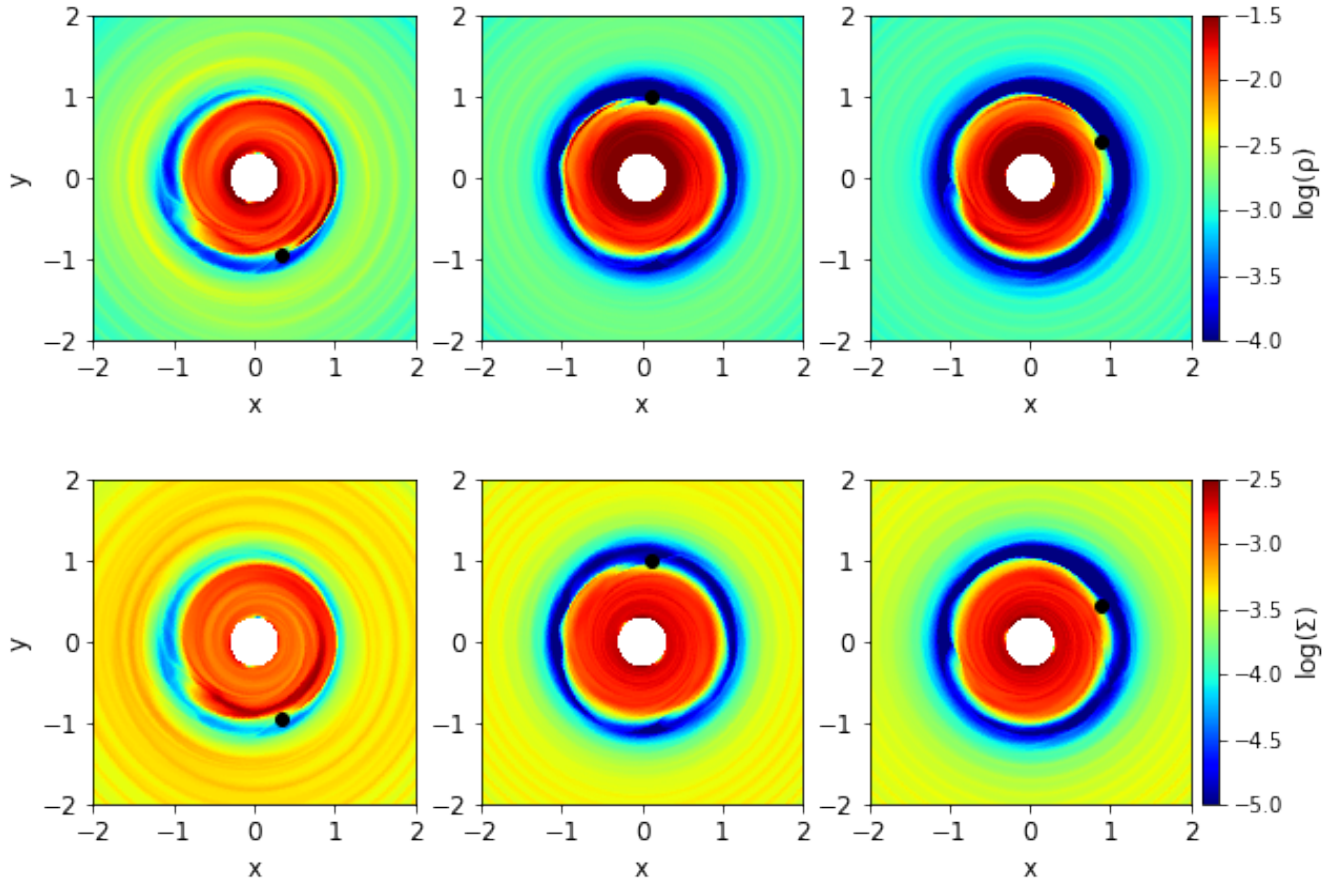


Figure 19. Volume density at $z = 0$ (upper panels) and surface density (lower panels) at 60, 690 and 1500 orbits (from left to right). The instantaneous position of the perturber is marked with a black circle. The perturber moves clockwise.

ACKNOWLEDGEMENTS

We thank the referee for thoughtful comments and suggestions. The numerical calculations were performed on the Miztli supercomputer at UNAM (project LANCAD-UNAM-DGTIC-03).

DATA AVAILABILITY

The FARGO3D code is available from <https://github.com/FARGO3D/fargo3d>. The output files of our hydrodynamical simulations will be shared on reasonable request to the corresponding author.

REFERENCES

- Artymowicz P., Lin D. N. C., Wampler E. J., 1993, *ApJ*, 409, 592
 Bate M. R., Lubow S. H., Ogilvie G. I., Miller K. A., 2003, *MNRAS*, 341, 213
 Bellovary J. M., Governato F., Quinn T. R., et al. 2010, *ApJ*, 721, L148
 Benítez-Llambay P., Masset F. S., 2016, *ApJS*, 223, 11
 Benítez-Llambay P., Krapp L., Pessah M. E., 2019, *ApJS*, 241, 25
 Cui Z., Papaloizou J. C. B., Szuszkiewicz E., 2021, *ApJ*, 921, 142
 de Val-Borro M., Edgar R. G., Artymowicz P. et al. 2006, *MNRAS*, 370, 529
 D’Angelo G., Kley W., Henning T., 2003, *ApJ*, 586, 540
 Davis S. W., Stone J. M., & Pessah M. E., 2010, *ApJ*, 713, 52
 Di Matteo T., Ni Y., Chen N., Croft R., Bird S., Pacucci F., Ricarte A., Tremmel M., 2023, *MNRAS*, 525, 1479
 Duffell P. C., 2015, *ApJ*, 807, L11
 Duffell P. C., MacFadyen A. I., 2013, *ApJ*, 769, 41
 Fung J., Shi J.-M., Chiang E., 2014, *ApJ*, 782, 88
 Fung J., Chiang E., 2016, *ApJ*, 832, 105
 Goldreich P., Tremaine S., 1980, *ApJ*, 241, 425
 Goodman J., Rafikov R. R., 2001, *ApJ*, 552, 793
 Hosseinbor A. P., Edgar R. G., Quillen A. C., Lapage A., 2007, *MNRAS*, 378, 966
 Imanishi M., Nakanishi K., Izumi T., Wada K., 2018, *ApJ*, 853, L25
 Impellizzeri C. M. V., Gallimore J. F., Baum S. A., et al. 2019, *ApJ*, 884, L28
 Ivanov P. B., Papaloizou J. C. B., Paardekooper S. -J., Polnarev A. G., 2015, *A&A*, 576, A29
 Kanagawa K. D., Muto T., Tanaka H., Tanigawa T., Takeuchi T., Tsukagoshi T., Momose M., 2016, *PASJ*, 68, 43
 Kanagawa K. D., Tanaka H., Muto T., Tanigawa T., Takeuchi T., 2015, *MNRAS*, 448, 994
 Kley W., 1999, *MNRAS*, 303, 696
 Kley W., D’Angelo G., Henning T., 2001, *ApJ*, 547, 457
 Kley W., Dirksen G., 2006, *A&A*, 447, 369
 Krolik J. H., 1999, *Active galactic nuclei: from the central black hole to the galactic environment*. Princeton University Press, Princeton, New Jersey, U.S.A.
 Lubow S. H., Seibert M., Artymowicz P., 1999, *ApJ*, 526, 1001
 Mastrobuono-Battisti A., Perets H. B., Loeb A., 2014, *ApJ*, 796, 40
 McKernan B., Ford K. E. S., Kocsis B., Lyra W., Winter L. M., 2014, *MNRAS*, 441, 900

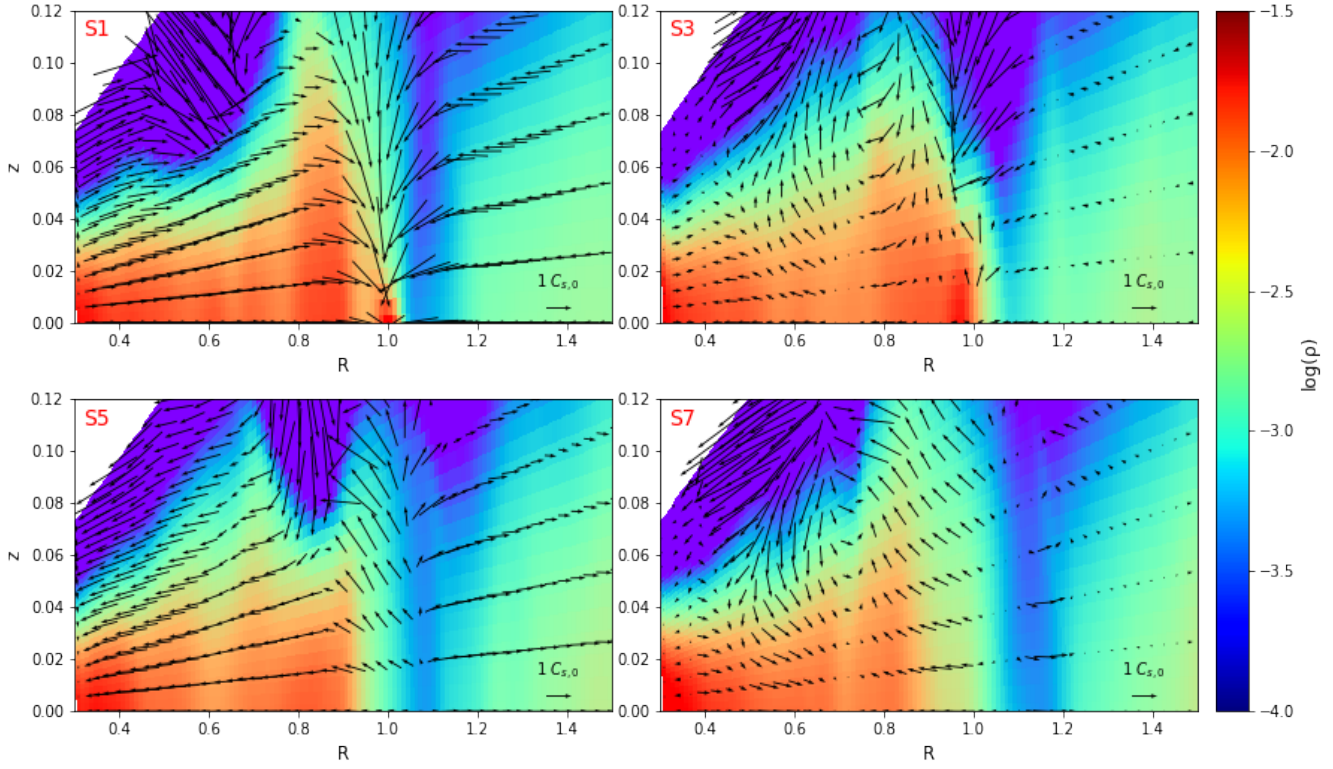


Figure 20. Meridional flow fields in four different sectors at $t = 60$ orbits. Background color represents volume gas density.

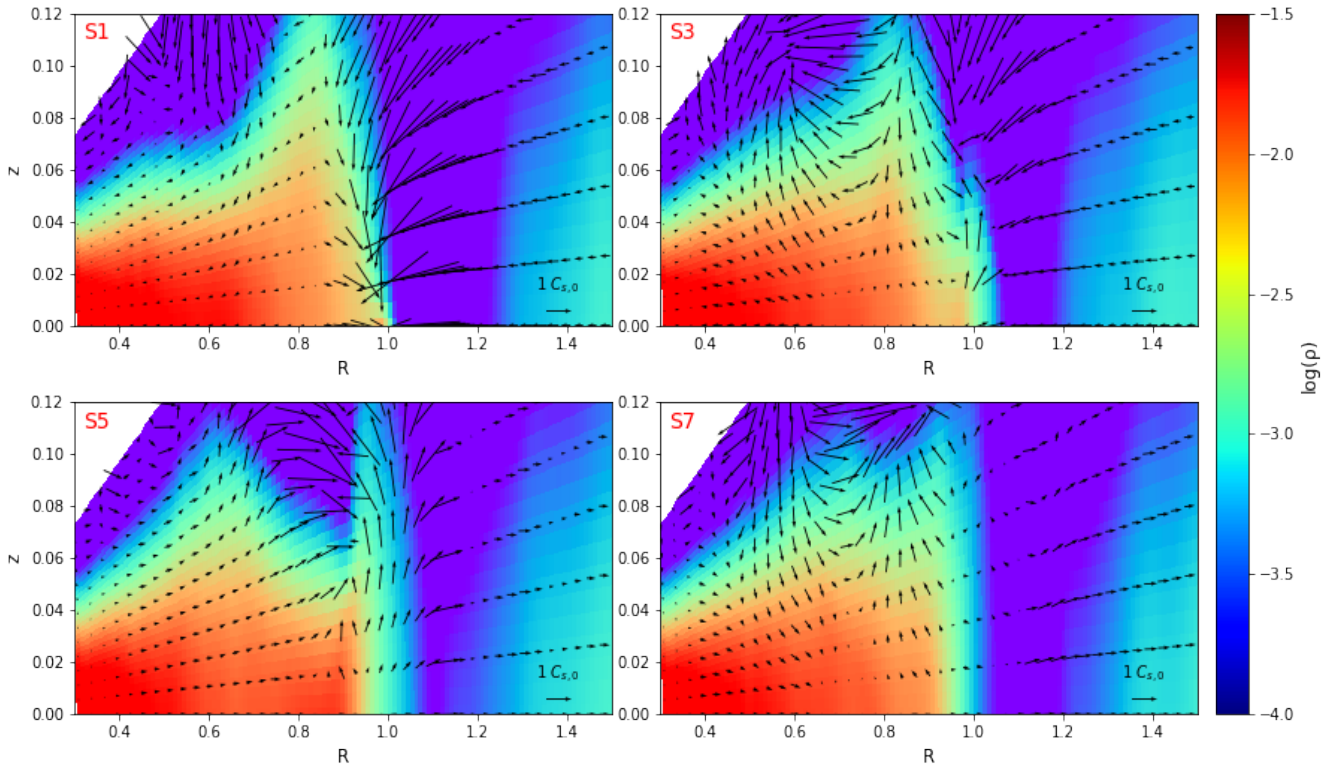


Figure 21. Same as Figure 20 but at $t = 1500$ orbits.

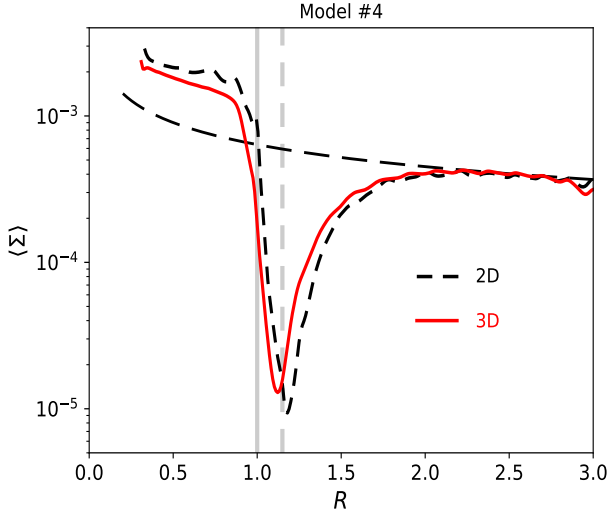


Figure 22. Azimuthally averaged surface density after 690 orbits in a 2D simulation (short dashed line) and in a 3D simulation (solid red line). The long dashed line corresponds to the initial surface density. For reference, the vertical solid grey line indicates $R = 1$ and the dashed grey line indicates $R = 1.15$.

- McKernan B., Ford K. E. S., Lyra W., Perets H. B., 2012, MNRAS, 425, 460
Muto T., Takeuchi T., Ida S., 2011, ApJ, 737, 37
Nasim S. S., Fabj G., Caban F., Secunda A., Ford K. E. S., McKernan B., Bellovary J. M., Leigh N. W. C., Lyra W., 2023, MNRAS, 522, 5393
Nelson R. P., Papaloizou J. C. B., 2003, MNRAS, 339, 993
Nixon C. J., King A. R., Pringle J. E., 2011, MNRAS, 417, L16
Ostriker J. P. 1983, ApJ, 273, 99
Overton M., Martin R. G., Lubow S. H., Lepp S., 2024, MNRAS, 528, L106
Peng P., Chen X., 2023, ApJ, 950, 3
Portegies Zwart S. F., McMillan S. L. W., 2002, ApJ, 576, 899
Portegies Zwart, S. F., Baumgardt H., McMillan S. L. W., Makino J., Hut P., Ebisuzaki T., 2006, ApJ, 641, 319
Sánchez-Salcedo F. J., 2020, ApJ, 897, 142
Sánchez-Salcedo F. J., Chametla R. O., Santillán A., 2018, ApJ, 860, 129
Secunda A., Bellovary J., Mac Low M.-M., et al. 2020, ApJ, 903, 133
Secunda A., Hernandez B., Goodman J., Leigh N. W. C., McKernan B., Ford K. E. S., Adorno J. I., 2021, ApJ, 908, L27
Sirko E., Goodman J., 2003, MNRAS, 341, 501
Snellgrove M. D., Papaloizou J. C. B., Nelson R. P., 2001, A&A, 374, 1092
Syer D., Clarke C. J., Rees M. J., 1991, MNRAS, 250, 505
Szölgén Á., Máthé G., Kocsis B., 2021, ApJ, 919, 140
Tagawa H., Kimura S. S., Haiman Z., Perna R., Bartos I., 2023, ApJ, 946, L3
Tanaka Y. A., Kanagawa K. D., Tanaka H., Tanigawa T., 2022, ApJ, 925, 25
Thompson T. A., Quataert E., Murray N., 2005, ApJ, 630, 167
Volonteri M., Haardt F., Madau P., 2003, ApJ, 582, 559
Yang Y., Bartos I., Gayathri V. et al. 2019a, Phys. Rev. Lett., 123, 181101
Yang Y., Bartos I., Haiman Z., Kocsis B., Márka Z., Stone N. C., Márka S., 2019b, ApJ, 876, 122

APPENDIX A: TORQUE ON THE PERTURBER IN THE LINEAR CASE

Two-dimensional disc models, which ignore the vertical size of the disc, are useful to quantify the contribution to the torque of density perturbations at distances $\gtrsim H$ from the perturber, which we denote by Γ_{2D} . It is convenient to introduce $F_{DF,0}$, defined as the dynamical friction force on a perturber moving supersonically in rectilinear orbit in a 2D slab of constant density Σ_0 . Using linear theory, [Muto et al.](#)

(2011) find that

$$F_{DF,0} = -\frac{\pi \Sigma_0 (GM_p)^2}{R_{\text{soft}} V_{\text{rel}}^2} \left(\frac{V_{\text{rel}}}{V_{\text{rel}}} \right), \quad (\text{A1})$$

where V_{rel} is the relative velocity of the perturber with respect to the gas. As said before, for a retrograde perturber in circular orbit, $V_{\text{rel}} \approx 2\Omega_p r_p$ and, therefore,

$$F_{DF,0} = \frac{\pi q^2 \Sigma_p \Omega_p^2 r_p^4}{4 R_{\text{soft}}} \quad (\text{A2})$$

in this case. Σ_p represents the disc surface density at the orbital radius of the perturber. It is useful to discuss the results in terms of the reference torque Γ_0 , defined as $\Gamma_0 = -r_p F_{DF,0}$.

[Sánchez-Salcedo et al. \(2018\)](#) show that, for low-mass perturbers, Γ_{2D} presents large oscillations with time because the perturber catch its own wake. In fact, during the time that the perturber takes to reach its own wake (π/Ω_p), the sound can only travel a distance πH , implying that the wake has not had time to spread. As a consequence of the interaction with its own wake, the time-averaged torque $\bar{\Gamma}_{2D}$ is smaller than Γ_0 (see Figure 6 in [Sánchez-Salcedo et al. 2018](#)). The formula for the torque derived in [Ivanov et al. \(2015\)](#) in linear theory predicts correctly the time averaged torque, and it can be approximated by

$$\bar{\Gamma}_{2D} = \lambda_{\mathcal{E}} \Gamma_0, \quad (\text{A3})$$

where

$$\lambda_{\mathcal{E}} \approx \frac{8\mathcal{E}}{\sqrt{3}} \left(\exp[-2\sqrt{3}\mathcal{E}] + \frac{2}{\sqrt{5}} \exp[-2\sqrt{5}\mathcal{E}] \right) + \frac{\sqrt{3}}{2} \frac{\exp(-12\mathcal{E})}{1 - \exp(-4\mathcal{E})}, \quad (\text{A4})$$

where $\mathcal{E} = R_{\text{soft}}/H$ ([Sánchez-Salcedo et al. 2018](#)). For a disc aspect ratio $h = 0.05$ and a softening parameter $\mathcal{E} = 0.6$, $\lambda_{\mathcal{E}} = 0.5$.

APPENDIX B: MIGRATING PERTURBERS

The backreaction of an eccentric disc on the perturber may lead to the excitation of the perturber's eccentricity. In this subsection we present the evolution of the semi-major axis a_p and orbital eccentricity e_p of the perturber when it is allowed to migrate freely under the influence of the gas drag. Initially, the perturbers are on a circular orbit with radius $r = 1$. The mass of the disc interior to this radius is $2.6 \times 10^{-3} M_{\odot}$. We first verified that, for $q = 0.001$ (linear case), the orbital migration rate matches the value predicted using the torque specified in Eq. (A3).

Figure B1 shows the evolution of a_p and e_p in models 3, 4 and 5, using outflow and damping IBCs. We have fitted the temporal evolution of the semi-major axis with an exponential function $a_p(t) = \exp(-t/t_a)$ (see dashed curves in the top panels of Fig. B1). Regardless of whether the IBCs are outflow or damping, the migration rate, t_a^{-1} , is higher in more viscous discs, as expected (e.g., [Ivanov et al. 2015](#)). Unlike in model 4, where the perturber migrates at the same rate with both outflow and damping IBCs, in models 3 and 5, the migration rate depends on the adopted IBCs.

It is remarkable that non-axisymmetric modes in the disc can excite the eccentricity of the perturber to values comparable to h . In models 3 and 4, the orbital eccentricity increases up to ~ 0.04 within the first 100 orbits, in both outflow and damping IBCs. The subsequent evolution of the orbiter's eccentricity, however, is sensitive to the choice of IBCs. The variations in e_p are caused by the phasing of the orbital eccentricity with respect to the disc eccentricity.

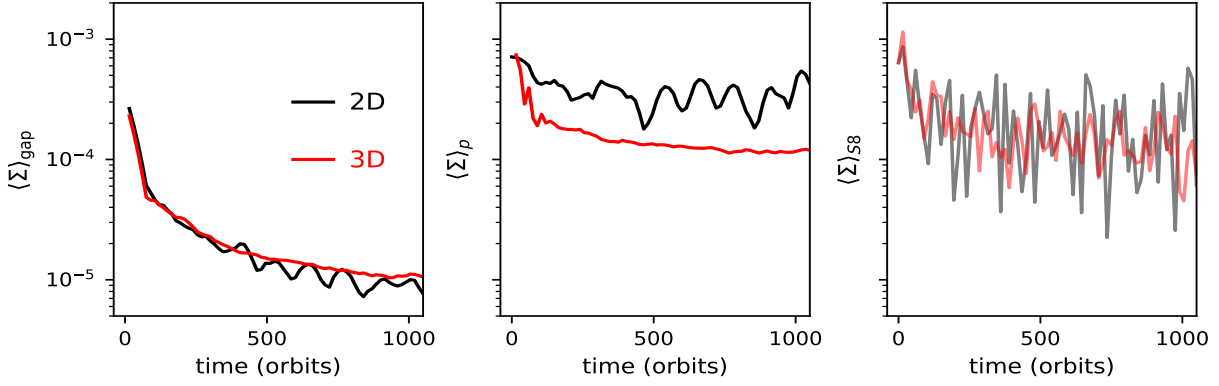


Figure 23. $\langle \Sigma \rangle_{\text{gap}}$ (left panel), $\langle \Sigma \rangle_p$ (central panel) and $\langle \Sigma \rangle_{S8}$ at $r = r_p$ (right panel) versus time for 2D (black line) and 3D simulations (red line) in model 4. Both simulations have the same domain size and number of cells in the radial and azimuthal directions.

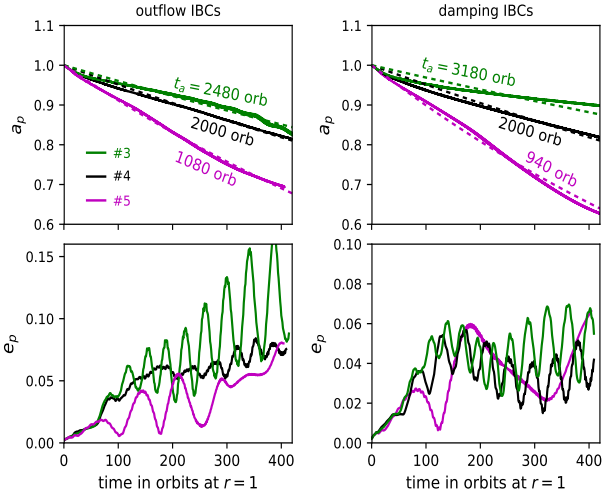


Figure B1. Semi-major axis (top panels) and eccentricity of the perturber (bottom panels) for migrating perturbers as obtained in the 2D simulations (solid lines). The dashed lines in the top panels represent an exponential decay fit: $a_p = \exp(-t/t_a)$. The values of t_a are provided as labels for each curve.

This paper has been typeset from a $\text{\TeX}/\text{\LaTeX}$ file prepared by the author.